

Numerical simulation of solitary gravity waves on deep water with constant vorticity

A. S. Dosaev,^{1, a)} M. I. Shishina,² and Yu. I. Troitskaya¹

¹⁾*Nonlinear Geophysical Processes Department, Institute of Applied Physics, Nizhny Novgorod, Russia*

²⁾*Nizhny Novgorod Planetarium n.a. G. M. Grechko, Nizhny Novgorod, Russia*

(Dated: 1 November 2022)

We present a numerical study of essentially nonlinear dynamics of surface gravity waves on deep water with constant vorticity using governing equations in conformal coordinates. The dispersion relation of surface gravity waves on shear flow is known to have two branches, one of which is weakly dispersive for long waves. Weakly nonlinear evolution of the waves of this branch can be described by the Benjamin-Ono equation, which is integrable and has soliton and multi-soliton solutions. Currently, the extent to which the properties of such solitary waves obtained within the weakly nonlinear model are preserved in the exact Euler equations is unknown. We investigate the behaviour of this class of solitary waves without the restrictive assumption of weak nonlinearity by using the exact Euler equations. The evolution of localized initial perturbations leading to the formation of single or multiple solitary waves is modeled, and the properties of finite-amplitude solitary waves are discussed. We show that within the framework of the exact equations, two-soliton collisions are almost elastic, but in contrast to solutions of the Benjamin-Ono equation the waves receive a phase shift as a result of the interaction.

I. INTRODUCTION

Waves in oceans or inland basins often propagate on vertically sheared currents, their dynamics being significantly affected by wave-current interaction¹. On vertically sheared currents, which may be produced by wind stress or bottom friction, the nonlinear properties of waves are modified, such as the rate of growth of modulational instability² or breaking conditions³. In particular, using perturbational analysis, Shrira observed⁴ that shear flows support a specific kind of solitary gravity wave that is absent in deep water without shear.

A special case, one for which theoretical treatment can be greatly simplified, is that of a two-dimensional flow with uniform shear (constant vorticity) because all perturbations to the velocity field are then strictly potential, as follows from Kelvin's circulation theorem. In this setting, many results concerning periodic and solitary stationary waves have been obtained numerically using the boundary integral method^{5–7}; the parameter space study was later extended by Vanden-Broeck^{8,9} to find more solution families. (See also a more recent study of periodic waves by S. Dyachenko and Hur^{10,11} that uses a conformal mapping technique.)

The scope of the present paper is confined to deep water waves on a uniform shear flow propagating in the direction of the shear (negative vorticity in our notation, see Section II). Such waves become weakly dispersive in the long wavelength limit, and their weakly nonlinear evolution is described by the Benjamin-Ono (BO) equation⁴. The BO equation is integrable and has stable soliton solutions; the solitons of the BO equation interact elastically and do not undergo a phase shift after the interaction^{12,13}. Our aim is to examine the behaviour of finite-amplitude solitary waves and to determine the extent

to which they retain the properties of their weakly-nonlinear counterparts. In contrast to the works on finite-amplitude waves cited above, we do not limit our study to stationary solutions; we use evolution equations to model solitary waves formation from a localized initial perturbation (which also ensures stability of the obtained waves), as well as interaction of two solitary waves.

The simulations are performed within the framework of the full Euler equations for deep water waves with constant vorticity. The governing equations in conformal coordinates for a constant vorticity flow with a free surface over an arbitrary bottom profile were obtained by Ruban¹⁴ and were independently obtained for a flat bottom by Choi¹⁵. Here we use a slightly different formulation that employs Dyachenko variables¹⁶ to improve numerical stability of the system; the corresponding governing equations were derived by Dosaev et al.¹⁷

Of high relevance to solitary waves modeling is also a recent development of the conformal mapping methodology related to the use of auxiliary conformal coordinates with adaptive resolution. Tanaka¹⁸ proposed a change in independent variables that allows to increase spatial resolution of the conformal grid in a neighborhood of a selected point (e.g., on the wave crest). Adaptive conformal coordinates were used to study linear stability of gravity waves^{18,19}, including waves with constant vorticity²⁰, and to obtain solutions with very steep profiles in some of the mentioned works on stationary waves^{10,11}. A detailed study by Lushnikov et al.²¹ has revealed that Hilbert transform can be computed on the adaptive grid as efficiently as it was in the original representation; the technique therefore integrates very naturally into the conventional conformal mapping approach. In the present work we employ adaptive coordinates to speed up stationary profile computation. Although applying the change in variables to the evolution equations is straightforward, too, a method for resolving arbitrary number of sharp profile features, as well as a robust strategy for dynamically adjusting the resolution

^{a)} Author to whom correspondence should be addressed: dosaev@ipfran.ru

during a simulation, still remains to be developed.

The paper is organized as follows. In Section II, we describe the physical model and introduce governing equations in conformal coordinates that we use in our simulations. In Section III, stationary wave profiles are obtained and their characteristics are compared with BO solutions. The results of numerical simulations are presented in Section IV: we model formation of solitary waves from disintegration of a localized perturbation, and study collision of two solitary waves using the profiles obtained in Section III. Section V summarizes the main results of the work.

II. BASIC EQUATIONS

A. Governing equations in Cartesian coordinates

Consider a two-dimensional flow of an ideal incompressible fluid with a free surface. In the (x, y) -plane, with the y -axis directed upward and the x -axis coinciding with the fluid surface at rest, we describe motion of the fluid using a stream function Ψ , which is connected to velocity components v_x, v_y as

$$v_x = \frac{\partial \Psi}{\partial y}, \quad v_y = -\frac{\partial \Psi}{\partial x}.$$

For waves propagating on a shear current with uniform vorticity distribution ($\omega = -\Delta \Psi = \text{const}$), the stream function can be decomposed into a sum

$$\Psi(x, y, t) = -\frac{\omega y^2}{2} + \psi(x, y, t),$$

where the first term, which corresponds to the rotational component of the velocity field, is time-independent and the perturbational part ψ satisfies $\Delta \psi = 0$.

The harmonic conjugate to ψ , which we denote φ , is defined by the Cauchy-Riemann conditions

$$\frac{\partial \varphi}{\partial x} = \frac{\partial \psi}{\partial y}, \quad \frac{\partial \varphi}{\partial y} = -\frac{\partial \psi}{\partial x},$$

and is the potential for the same velocity perturbation defined by the stream function ψ :

$$v_x = -\omega y + \frac{\partial \varphi}{\partial x}, \quad v_y = \frac{\partial \varphi}{\partial y}.$$

Together φ and ψ form a “complex potential”, $\theta = \varphi + i\psi$, which is an analytic function of a complex variable $z = x + iy$ in the flow domain.

At the free surface $y = f(x, t)$, kinematic and dynamic boundary conditions must be satisfied:

$$\frac{\partial f}{\partial t} + \left(-\omega f + \frac{\partial \varphi}{\partial x} \right) \frac{\partial f}{\partial x} - \frac{\partial \varphi}{\partial y} = 0, \quad (1)$$

$$\frac{\partial \varphi}{\partial t} + \frac{1}{2} |\nabla \varphi - \omega y \mathbf{x}_0|^2 + \omega \psi - \frac{\omega^2 y^2}{2} + \frac{p_a}{\rho} + gy = 0, \quad (2)$$

where \mathbf{x}_0 is a unit vector in the direction of the x -axis, g is the gravity acceleration, and p_a is pressure at the free surface. Inside the flow domain, φ must satisfy the Laplace equation

$$\Delta \varphi = 0. \quad (3)$$

We confine our study to deep water waves, thus assuming a boundary condition at infinity:

$$|\nabla \varphi| \rightarrow 0 \quad \text{as} \quad y \rightarrow -\infty. \quad (4)$$

Set (1)–(4) is equivalent to exact Euler equations and completely defines dynamics of the system.

For small amplitude waves propagating in the positive direction of the x -axis, the system (1)–(4) gives the following dispersion relation:

$$c^2 k - \omega c - g = 0, \quad (5)$$

where k is the wavenumber and c is the phase velocity. The parameters of the system, g and ω , have only one combination with dimension of length

$$\lambda_g = g/\omega^2,$$

which is therefore a natural length scale for the problem. According to (5), long waves ($k\lambda_g \ll 1$) propagating in the direction of shear (i.e. in the positive direction of the x -axis, if $\omega < 0$) are weakly dispersive:

$$c \approx \frac{g}{|\omega|} - \frac{gk}{|\omega|^3} = c_0(1 - k\lambda_g), \quad (6)$$

where $c_0 = g/|\omega|$ is the limiting phase velocity for small-amplitude long waves. The weakly nonlinear evolution of such long waves is described by the Benjamin-Ono equation⁴

$$\left(\frac{\partial}{\partial t} + c_0 \frac{\partial}{\partial x} \right) f - \omega f \frac{\partial f}{\partial x} - \frac{g^2}{\omega^3} \hat{H} \frac{\partial^2 f}{\partial x^2} = 0, \quad (7)$$

where \hat{H} is Hilbert transform:

$$\hat{H}f(x) = \frac{1}{\pi} P.V. \int_{-\infty}^{+\infty} \frac{f(\chi) d\chi}{\chi - x}.$$

B. Governing equations in conformal coordinates

Let us map the flow domain onto a lower half-plane of complex variable $\zeta = \xi + i\eta$ via a (time-dependent) conformal mapping

$$x + iy = z(\zeta, t) = \xi + i\eta + \tilde{x}(\xi, \eta, t) + i\tilde{y}(\xi, \eta, t).$$

The free surface $y = f(x, t)$ is thus mapped onto the real axis $\eta = 0$.

The resulting parameterization of the free surface is particularly convenient because in the new coordinates (ξ, η) functions φ and ψ remain harmonic, and their values on the free surface $\eta = 0$ are related through the Hilbert transform

$$\psi(\xi, \dots) = \hat{H}\varphi(\xi, \dots).$$

In conformal coordinates, boundary conditions (1) and (2) at the free surface $\eta = 0$ become^{15,22}

$$x_\xi y_t - x_t y_\xi = -\hat{H}\varphi_\xi + \omega y y_\xi, \quad (8)$$

$$\begin{aligned} \varphi_t + \varphi_\xi \hat{H} \left[\frac{-\psi_\xi + \omega y y_\xi}{J} \right] - \frac{\omega y x_\xi}{J} \varphi_\xi \\ + \frac{\varphi_\xi^2 - \psi_\xi^2}{2J} + \omega \psi + \frac{p_a}{\rho} + g y = 0, \end{aligned} \quad (9)$$

where $J = |z_\xi|^2$. They can also be written in terms of analytical functions z and θ as

$$z_t = iU z' \quad (10)$$

$$\begin{aligned} \theta_t = iU \theta' - (1 + i\hat{H}) \left(\frac{|\theta'|^2}{2|z'|^2} - \omega y \operatorname{Re} \frac{\theta'}{z'} + \frac{p_a}{\rho} \right) \\ + i\omega \theta + ig(z - \xi), \end{aligned} \quad (11)$$

where prime denotes differentiation with regard to ζ , and

$$U = (1 + i\hat{H}) \left[\frac{-\psi_\xi + \omega y y_\xi}{J} \right].$$

For the purpose of modeling the evolution of the system, the equations (10) and (11) can be rewritten in a form, that is more suitable for numerical integration, through a change of variables

$$R = \frac{1}{z'}, \quad V = \frac{i\theta'}{z'}. \quad (12)$$

The resulting governing equations are as follows¹⁷:

$$R_t = i(UR' - U'R) \quad (13)$$

$$\begin{aligned} V_t = i \left(UV' - R\hat{P}'(|V|^2 - 2\omega \operatorname{Im} z \operatorname{Im} V + \frac{2p_a}{\rho}) \right) \\ + g(R - 1) + i\omega V, \end{aligned} \quad (14)$$

where $\hat{P} = \frac{1}{2}(1 + i\hat{H})$ is a projection operator, and

$$U = \hat{P}(RV^* + R^*V - 2\omega \operatorname{Im} z \operatorname{Im} R).$$

When $\omega = 0$, system (13) and (14) is reduced to the Dyachenko equations¹⁶. In the rest of this work the external pressure p_a is assumed to be zero.

Derivation of the BO equation in conformal coordinates is given in the Appendix.

III. FINITE-AMPLITUDE STATIONARY WAVES

In this section we obtain periodic stationary solutions of the exact equations of motion and discuss what new properties they possess compared to the weakly nonlinear BO model. Our interest to the periodic solutions in the context of solitary waves stems from the fact that BO solitons are algebraic

with $f \sim x^{-2}$ tails; they, therefore, cannot be represented with reasonable precision on a periodic coordinate grid that our numerical scheme (based on fast Fourier transform) utilizes. As a result, we must limit ourselves to studying periodic solutions, approaching solitary waves through increase in spatial period.

Periodic solution of the BO equation takes the form²³

$$\begin{aligned} f(x, t) = f_0 + \frac{akd}{4i} \left(\cot \frac{k}{2}(x - ct - id) \right. \\ \left. - \cot \frac{k}{2}(x - ct + id) \right), \end{aligned} \quad (15)$$

where $k = 2\pi/L$ is the wavenumber and the parameters satisfy

$$ad = 4\lambda_g^2, \quad (16)$$

$$c = c_0 + |\omega|f_0 + \frac{|\omega|a}{4}kd \coth kd.$$

The crest becomes more localized as the wave “amplitude” a increases, and in the limit $kd \rightarrow 0$ the profile becomes Lorentzian:

$$f(x, t) = \frac{a}{1 + (x - ct)^2/d^2}, \quad (17)$$

$$c = c_0 + \frac{|\omega|a}{4}. \quad (18)$$

In order to obtain an equation for the exact stationary wave profile in conformal coordinates we seek solutions for (8) and (9) in the form

$$y = y(\xi - ct), \quad x = \xi + \tilde{x}(\xi - ct), \quad \varphi = \tilde{\varphi}(\xi - ct) - gb_0 t.$$

Substitution into (8) gives

$$(c + \omega y)y_\xi = \hat{H}\varphi_\xi. \quad (19)$$

Using (19), we eliminate potential φ from (9) and obtain an equation for the wave profile in conformal parameterization $z(\xi)$:

$$gy - gb_0 = \frac{c^2}{2} - \frac{(c + \omega(yx_\xi + \hat{H}(yy_\xi)))^2}{2J}. \quad (20)$$

Equations of motion (1)–(4) contain only two parameters of the medium, that is, g and ω , and exactly two parameters we can exclude from the equations by choosing appropriate units of measurement for length and time. This means that the nondimensionalized form of the equations obtained by converting to nondimensionalized coordinates and time

$$X = x/\lambda_g, \quad Y = y/\lambda_g, \quad \Xi = \xi/\lambda_g, \quad T = |\omega|t$$

will not contain any parameters that depend on the medium, and a similarity law can be established for motions of the system at various (g, ω) . Therefore, profiles of stationary waves that for $\omega < 0$ satisfy a nondimensionalized equation

$$Y + \frac{1}{2J} (C - YX_\Xi - \hat{H}(Y Y_\Xi))^2 = \text{const}$$

are universal and only depend on dimensionless phase velocity $C = c/c_0$ and wavelength $\Lambda = L/\lambda_g$. Solitary waves, which can be considered a special case of a stationary wave with infinite wavelength, constitute a one-parameter family of solutions, and all of their dimensionless parameters (such as wave height h/λ_g or phase velocity c/c_0) can be found as functions of a single parameter.

We seek a solution to (20) in a form of a pole expansion

$$z(\zeta) - \zeta = z_0 + \sum_n a_n \frac{kd_n}{2} \cot \frac{k}{2} (\zeta - id_n). \quad (21)$$

where the constant $z_0 = iy_0$ is chosen so that the mean water level remains zero:

$$\int y x_\xi d\xi = 0.$$

If all $d_n > 0$, then $z(\zeta)$ only has poles in the upper half-plane, and is analytical in the flow domain $\text{Im } \zeta < 0$. For a given phase velocity c we can obtain the optimal set of coefficients $\{a_n, d_n\}$ by minimizing the residual of the stationary wave equation (20):

$$r(a_1, \dots, d_1, \dots) = gy + \frac{(c + \omega(yx_\xi + \hat{H}(yy_\xi)))^2}{2J} - \frac{c^2}{2},$$

$$\int |r|^2 du \rightarrow \min.$$

We use fast Fourier transform to compute the derivatives and Hilbert transform. Number of points of the spatial grid required for the computation of the residual can be greatly reduced by utilizing an adaptive conformal grid²¹ with increased resolution in the vicinity of the wave crest. The adaptive grid is equidistant in an auxiliary coordinate q :

$$\frac{\xi}{2} = \arctan \left(\alpha \tan \frac{q}{2} \right).$$

Hilbert transform, computed in the q coordinate, differs from that in the ξ coordinate only by a constant, which can be easily found from the condition that mean value of the transform in the corresponding coordinate is zero. After obtaining profile (21), the corresponding velocity field is recovered from (19). This stationary solution in form of $z(\xi)$ and $\varphi(\xi)$ can also be converted to Dyachenko representation according to (12), which will be used in Section IV for constructing initial conditions for numerical simulations.

Using this simple method and by varying spatial period L and phase velocity c , we were able to obtain waves of any height up to the point of phase velocity extremum (which is located around $h \approx 0.55\lambda_g$ for long waves $L > 10^3\lambda_g$). Here the wave height is defined as

$$h = \max_x f - \min_x f = \max_\xi y - \min_\xi y.$$

Less than 10 poles in the expansion (21) were typically required to achieve the best approximation, further minimization of the residual being obstructed by numerical errors in its

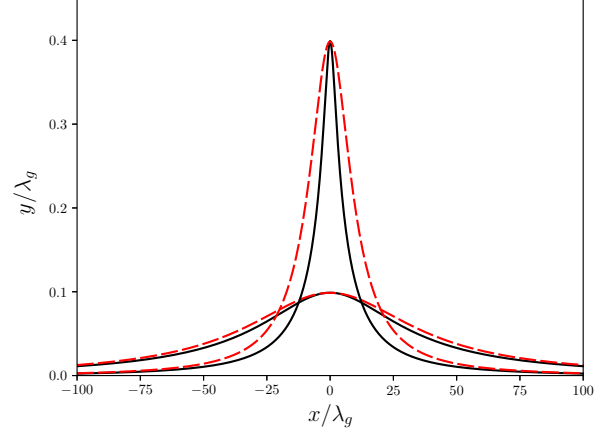


FIG. 1: Stationary waves of the exact equations (solid lines) and the BO solutions of the same height (dashed lines). Wave heights: $h = 0.1\lambda_g$, $0.4\lambda_g$, wavelength $L = 10^4\lambda_g$.

computation (within IEEE 754 double precision). The considered range of amplitudes contains a maximum of wave energy (see below), which means that only part of the range represents stable solutions. Since our primary goal is to study solitary wave interactions, only stable solutions are of interest in the context of this work.

Figure 1 shows example profiles of stationary waves with heights $h = 0.1\lambda_g$, $0.4\lambda_g$ and wavelength $L = 10^4\lambda_g$, together with periodic BO profiles with the same parameters. Such long waves already have a great resemblance to solitons, because for the profiles in the figure the crest widths at half maximum constitute less than 0.01 of the wave period. One can see that although the exact and BO solutions are very similar at $h = 0.1\lambda_g$, for higher waves the crests of the exact profiles become noticeably more narrow and sharp than the crests of their BO counterparts, despite both profiles having very close asymptotics at large distances from the crest.

To better illustrate this observation we introduce profile “volume”, which we define as:

$$S = \int_{-L/2}^{L/2} f(x) dx - L \min_x f(x)$$

According to (16), the volume of BO solitons (as well as very high periodic waves) does not depend on wave amplitude and is equal to $S_{BO} = 4\pi\lambda_g^2$. Profile volume S as a function of wave height h for various wave periods L is plotted in figure 2a; as the figure shows, exact profiles do not just have a different shape of their crests, but also their volume is decreasing at high amplitudes.

We define wave energy E as the excess of mechanical energy due to the presence of the wave:

$$E = \frac{g}{2} \int y^2 x_\xi d\xi - \frac{1}{2} \int \varphi \hat{H} \varphi_\xi d\xi + \frac{\omega^2}{6} \int y^3 x_\xi d\xi + \omega \int \varphi y y_\xi d\xi. \quad (22)$$

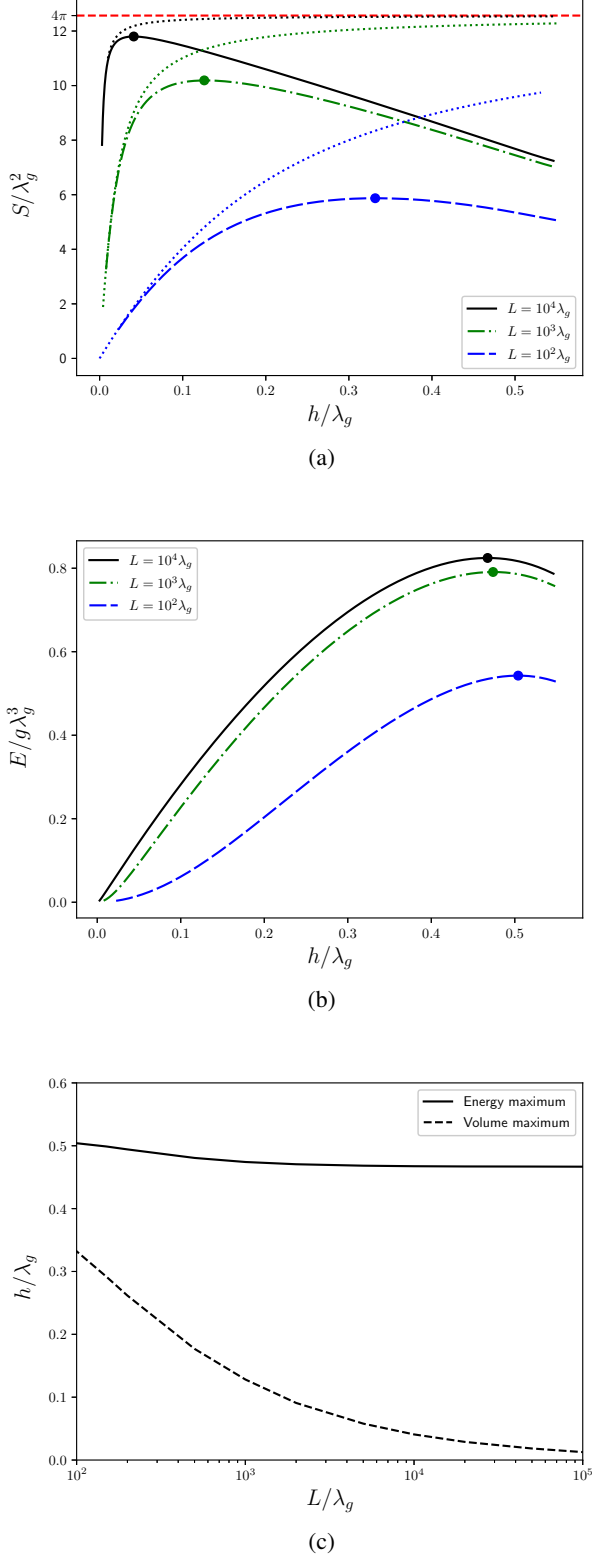


FIG. 2: (a) Profile volume and (b) wave energy as functions of wave height; dotted lines represent volume of the BO solutions and markers show locations of maxima for solutions of the exact equations. (c) Positions of energy and volume maxima as functions of wave period.

It is shown in figure 2b as a function of wave height for various values of wave period. As the figure shows, energy attains a maximum at some critical height, which depends on the wavelength L . Waves of greater height are unstable — this is in contrast with BO solitons, which are stable for all amplitudes. The associated superharmonic instability was studied for waves on linear shear current by Murashige and Choi²⁰. Positions of energy and volume extrema as functions of wave length L are shown in figure 2c; as one can see, the critical height changes very little with increase of L , approaching $h \approx 0.467\lambda_g$ for long waves.

IV. NUMERICAL SIMULATIONS

In this section we study dynamic behaviour of solitary waves, including their formation from an initial perturbation and interaction of two solitary waves. To model the dynamics of the system (1)–(4), we integrate numerically the governing equations in conformal coordinates (13) and (14) with periodic boundary conditions using the fifth order Dormand–Prince method of the Runge-Kutta family with a built-in error estimate.

A. Disintegration of a localized perturbation

In order to observe solitary wave formation from an initial perturbation we prescribed the initial conditions in a form of a Lorentzian pulse

$$f(x) = \frac{a}{1 + x^2/d^2} W(x), \quad W(x) = \cos^2 \frac{\pi x}{L}, \quad (23)$$

where a window function $W(x)$ was introduced to smooth a jump of derivatives at the ends of the global period. Height a and half-width at half-maximum d of the pulse were changed independently, without being necessarily bound by (16). The velocity profile was prescribed according to (19), with the phase velocity c computed using (18) for the soliton of the same height a . In all experiments, the global spatial period $L = 10^4 \lambda_g$ was at least 10^2 times greater than the initial pulse width d .

As a result of disintegration of pulses (23) with various parameters, single or multiple solitary waves, as well as packages of oscillatory waves were typically formed. An example in figure 3 shows how the disintegration of a pulse with width more than three times greater than that of a BO soliton of the same height leads to formation of multiple solitons. Figure 4 shows how parameters of generated waves depend on parameters of initial disturbance. A noteworthy feature of these results is that for a wide range of initial heights the disintegration products of pulses, whose parameters *do* satisfy (16), seem to accumulate in the vicinity of height $0.42\lambda_g$ (which is also slightly less than the critical height). We did not conduct a parameter space study detailed enough to tell whether this is a general behaviour for a wider class of initial conditions. In figure 5 half-widths at half-maximum d of the formed solitary waves and their phase velocities c are plotted against wave

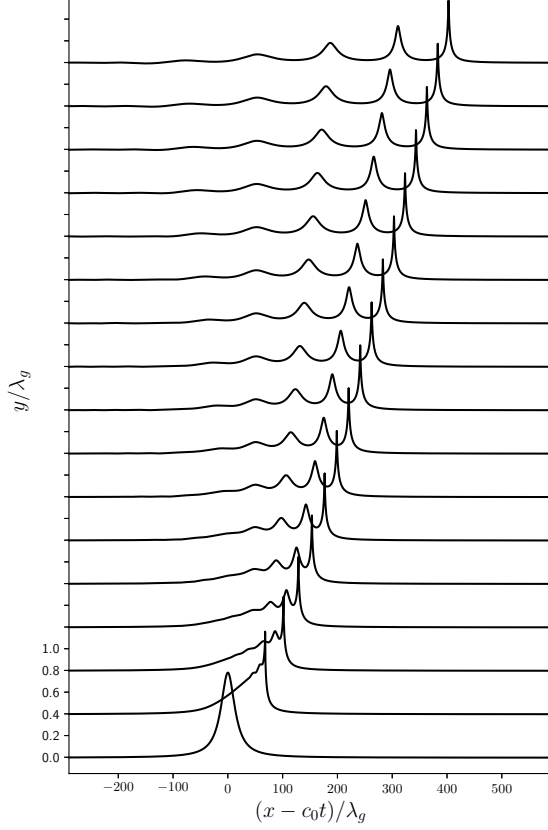


FIG. 3: Disintegration of a Lorentz pulse with height $a = 0.78\lambda_g$ and width $d = 15.3\lambda_g$, and the subsequent formation of three solitary waves; global period $L = 10^4\lambda_g$, time step between snapshots $|\omega|\Delta t = 186$, lower profiles correspond to earlier stages.

height; as the figure shows, parameters of generated waves are in reasonable agreement with the parameters of stationary waves, obtained in Section III.

B. Solitary wave collisions

To prepare initial conditions containing two waves at the prescribed positions $\{x_{0n}\}$ we combine individual wave profiles with phase velocities $\{\tilde{c}_n\}$ as

$$\begin{aligned} R(\xi) &= 1 + \sum_{n=1,2} (R_n(\xi - x_{0n}) - 1), \\ V(\xi) &= \sum_{n=1,2} V_n(\xi - x_{0n}). \end{aligned} \quad (24)$$

where R_n, V_n are the Dyachenko representation (12) of the stationary wave profiles, obtained in Section III. Phase velocity of waves with constant vorticity is affected by mean water level; in our setup, where the mean level is kept zero both for periodic stationary waves and for the superposition (24), the

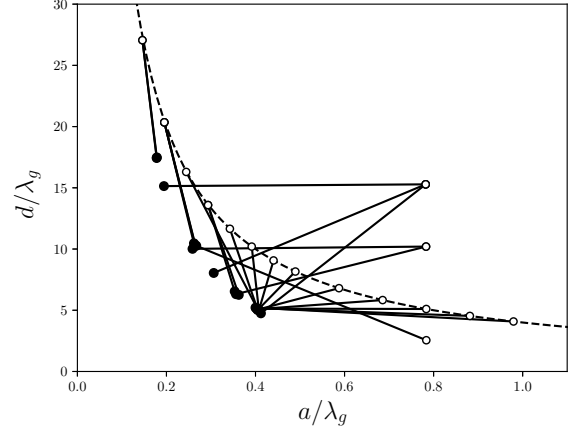


FIG. 4: Parameters of initial Lorentzian pulses (a and d , white markers) and characteristics of solitary waves formed as a result of their disintegration (height h and half-width at half-maximum d , black markers). Edges show the relation between the initial conditions and the products. Dashed line corresponds to equation (16).

actual observed phase velocities of the crests in the superposition will differ slightly from the original values $\{\tilde{c}_n\}$, and will be approximately equal to $c_{1,2} \approx \tilde{c}_{1,2} + \omega S_{2,1}/L$, where $S_{1,2}$ are volumes of the wave profiles.

Since individual stationary waves have slowly decreasing power-law tails, it is infeasible within our model to start the simulation from a point, where interaction between the waves is negligible. We must therefore study how the result of the interaction depends on initial distance between the crests $\Delta L_0 = x_{02} - x_{01}$.

We are considering only waves propagating in the direction of the shear, therefore a collision can only occur when a higher and faster solitary wave catches up with a lower and slower one. Hereinafter we will use index $n = 1$ to refer to the higher solitary wave, and $n = 2$ — to the lower wave. We examine three sets of wave heights: 1) two low solitary waves: $h_1 = 0.15\lambda_g$, $h_2 = 0.05\lambda_g$, 2) one wave is high, and the other is low: $h_1 = 0.40\lambda_g$, $h_2 = 0.10\lambda_g$, and 3) two high waves: $h_1 = 0.40\lambda_g$, $h_2 = 0.30\lambda_g$. For each pair of wave heights a number of simulations were performed with varying global period L and initial distance ΔL_0 . Each simulation started at $t = 0$ with the initial conditions (24), and continued until $t = 2t_c$, where $t_c = \Delta L_0 / (c_1 - c_2)$ is the time when the collision is expected to occur. We required that L and ΔL_0 satisfy

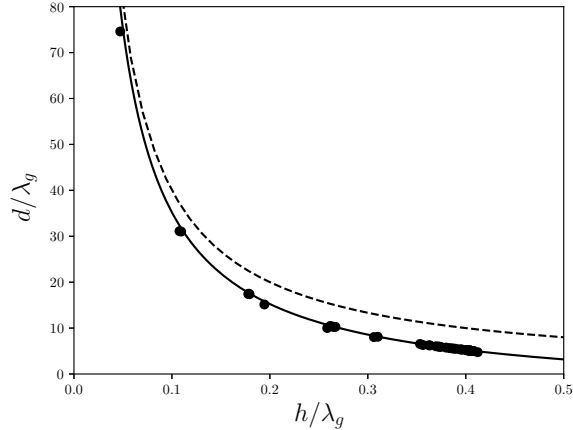
$$\frac{2\Delta L_0}{c_1 - c_2} < \frac{L}{c_1 - c_0}$$

so that until the end of simulation (i.e., until the two waves are again separated by the initial distance ΔL_0) the faster wave would not catch up with any artifacts that were excited at the moment $t = 0$ by the “artificial” superposition (24).

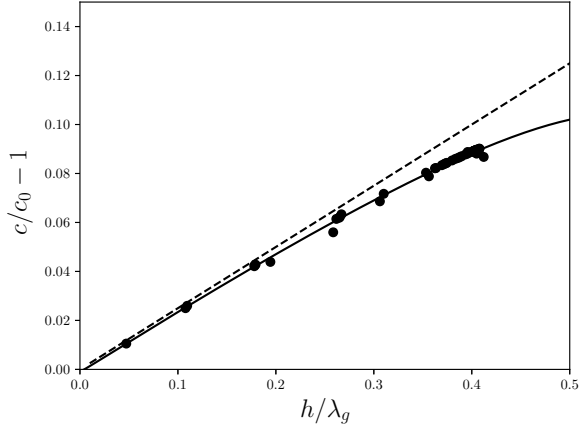
The results of the numerical simulations, which include parameters of the setup (global period L and initial distance be-

| h_1 | h_2 | ΔL_0 | L | ΔL_{min} | Δx_1 | Δx_2 | h'_1 | h'_2 |
|--------|--------|-----------------|------------------|------------------|--------------|--------------|--------|--------|
| 0.1501 | 0.0500 | $2 \cdot 10^3$ | $50 \cdot 10^3$ | 151.97 | -23.41 | -10.40 | 0.1501 | 0.0497 |
| 0.1500 | 0.0500 | $4 \cdot 10^3$ | $50 \cdot 10^3$ | 152.84 | -32.87 | -5.18 | 0.1500 | 0.0499 |
| 0.1500 | 0.0500 | $8 \cdot 10^3$ | $50 \cdot 10^3$ | 153.06 | -36.96 | -2.24 | 0.1500 | 0.0499 |
| 0.1500 | 0.0500 | $16 \cdot 10^3$ | $100 \cdot 10^3$ | 153.11 | -39.70 | -0.60 | 0.1500 | 0.0499 |
| 0.1500 | 0.0500 | $32 \cdot 10^3$ | $100 \cdot 10^3$ | 153.13 | -41.62 | 0.27 | 0.1500 | 0.0499 |
| 0.4000 | 0.1000 | $2 \cdot 10^3$ | $20 \cdot 10^3$ | 58.48 | -103.79 | -0.30 | 0.4027 | 0.0966 |
| 0.4000 | 0.1000 | $4 \cdot 10^3$ | $20 \cdot 10^3$ | 58.56 | -108.63 | -0.90 | 0.4028 | 0.0978 |
| 0.4000 | 0.1000 | $8 \cdot 10^3$ | $50 \cdot 10^3$ | 58.58 | -111.84 | -1.61 | 0.4028 | 0.0980 |
| 0.4000 | 0.3000 | $2 \cdot 10^3$ | $50 \cdot 10^3$ | 242.42 | -64.67 | -79.53 | 0.4004 | 0.2998 |
| 0.4000 | 0.3000 | $4 \cdot 10^3$ | $50 \cdot 10^3$ | 243.87 | -87.61 | -69.08 | 0.4003 | 0.2998 |

TABLE I: Phase shifts and amplitudes of solitary waves after the collision. All values are given in units of λ_g .



(a)



(b)

FIG. 5: Characteristics of solitary waves vs wave height h : (a) half-width at half-maximum; (b) phase velocity. Markers correspond to solitary waves formed as a result of initial disturbance disintegration, solid lines — to solutions of exact equations (with the same spatial period $L = 10^4 \lambda_g$), dashed lines — to BO solitons.

tween the waves ΔL_0), amplitudes of the waves before ($h_{1,2}$ at $t = 0$) and after the collision ($h'_{1,2}$ at $t = 2t_c$), minimal distance between the waves during the interaction ΔL_{min} and phase shifts $\Delta x_{1,2}$, are given in table I.

All three mentioned pairs of wave heights turned out to demonstrate an exchange scenario of interaction. When amplitude of the second wave is sufficiently small, an overtaking also becomes possible; we observed this behavior, for example, for a pair $h_1 = 0.35\lambda_g$ and $h_2 = 0.02\lambda_g$. We did not study overtaking scenario in greater detail.

The method of measuring the phase shifts requires special attention, because even small discrepancy in the involved values of phase velocity can lead, over long time intervals, to a large inaccuracy in the resulting phase shift values. We also need to take into account the possibility for the phase velocity after the collision to be slightly different from the initial velocity, due to the interaction being inelastic. We therefore adopted the following definition for the phase shift, based on the actual velocity of the solitary wave crest

$$\Delta x_n = [x_n(2t_c) - x_n(0)] - [\dot{x}_n(0) + \dot{x}_n(2t_c)]t_c \quad (25)$$

where $x_n(t)$ is the observed trajectory of the n -th wave (defined as the position of the local elevation maximum), $\dot{x}_n(t)$ — its velocity. This is equivalent to measuring position of the crest relative to the reference trajectory

$$x_n^R(t) = \begin{cases} x_n(0) + \dot{x}_n(0)t, & t \leq t_c \\ x_n(0) + \dot{x}_n(0)t_c + \dot{x}_n(2t_c)(t - t_c), & t > t_c \end{cases} \quad (26)$$

that is, $\Delta x_n = x_n(2t_c) - x_n^R(2t_c)$.

The phase shift definition (25), which uses only a finite piece of the wave trajectory in the vicinity of the collision point, would actually produce non-zero values even for the two-soliton solution of the BO equation (although the “apparent” phase shifts of the BO solitons vanish at large observation times). This is mostly due to the fact, that the faster soliton “jumps” forward during the exchange (and the slower one “jumps” backward). In figure 6 the measured phase shifts in the numerical simulations are plotted against the initial distance ΔL_0 ; apparent phase shifts for the two-soliton BO solution¹³, computed as in (25) for the same pair of soliton amplitudes and the same initial distance ΔL_0 , are plotted as a reference. As the figure shows, in the first (low+low pair)

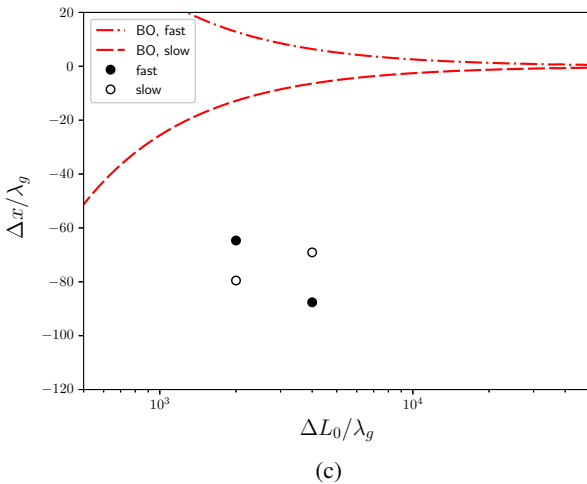
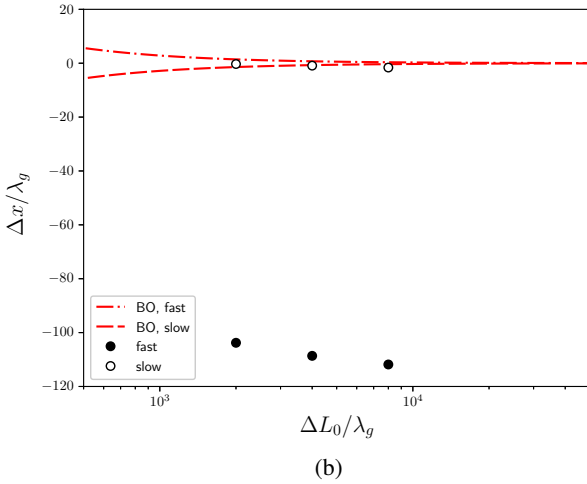
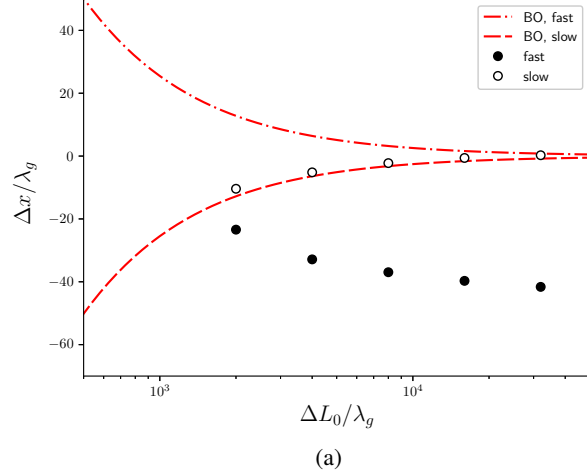


FIG. 6: Phase shifts of solitary waves vs initial distance. The parameters: (a) $h_1 = 0.15\lambda_g$, $h_2 = 0.05\lambda_g$, (b) $h_1 = 0.40\lambda_g$, $h_2 = 0.10\lambda_g$ and (c) $h_1 = 0.40\lambda_g$, $h_2 = 0.30\lambda_g$.

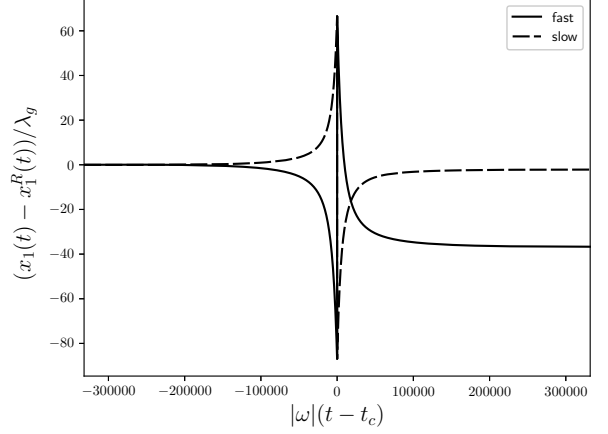


FIG. 7: Accumulation of the phase shift of the faster solitary wave (solid line) and the slower one (dashed line) during the interaction. The parameters: $h_1 = 0.15$, $h_2 = 0.05$, $\delta L_0 = 8000\lambda_g$, $L = 50 \cdot 10^3\lambda_g$

and the second (high+low) series of simulations phase shifts of the slower solitary waves closely resemble the behaviour of the apparent phase shifts of the slower solitons in the BO two-soliton solution, and approach (for low+low) or stay in the vicinity of zero (for high+low) as ΔL_0 increases. Meanwhile, phase shifts of the faster waves grow in absolute value, approaching constant negative levels. Figure 7 shows a typical example of how the position of the faster solitary wave relative to the reference trajectory (26) changes over time; one can see, that the phase shift is developed shortly after the collision, remaining almost constant until the end of the simulation.

Unfortunately, we were not able to conduct many experiments for the third pair of solitary waves (high+high) due to the simulation cost being much greater for that pair than for the first two. Still, from the available points in figure 6c it is already clear that in this pair the behaviour of the slower wave departs from the predictions of the BO equation as prominently as the behaviour of the faster one does.

Finally, figure 8 shows generation of a small-amplitude step-like perturbation on the free surface after the collision of a pair of high solitons, which indicates the inelastic nature of the solitary waves interaction. This feature is absent in the two-soliton solution of the BO equation, which at all times is represented by a sum of two poles. However, as indicated in the Table I, in all our simulations the wave amplitudes after the collision remain close to the initial amplitudes, from which we can conclude that the interaction is almost elastic.

V. CONCLUSIONS

The existence of solitons on deep water with constant vorticity propagating in the direction of the shear was demonstrated in earlier research (see Shrira⁴) in the limit of large wavelengths (i.e., weak dispersion) and small amplitudes. It

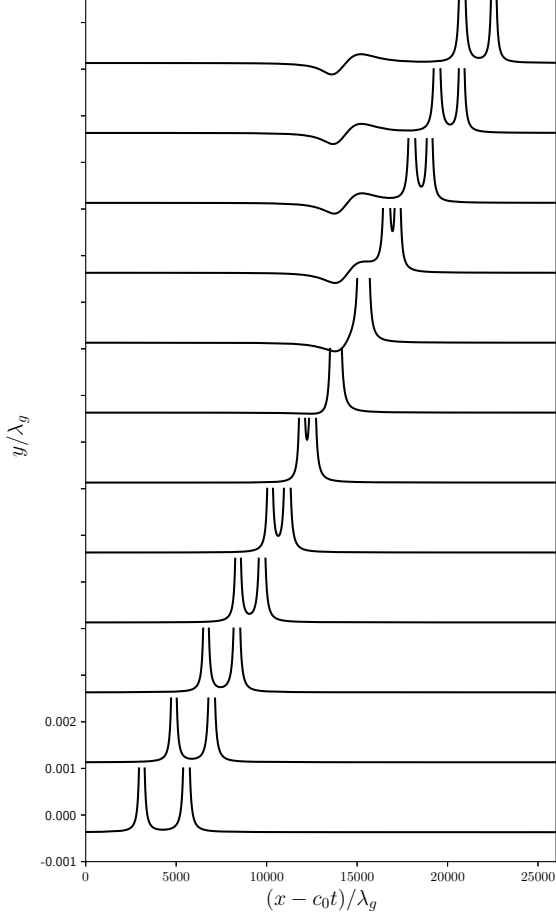


FIG. 8: Generation of a step-like perturbation on the free surface after a collision of two solitons. The parameters: $h_1 = 0.4\lambda_g$, $h_2 = 0.3\lambda_g$, and $\Delta L_0 = 4000\lambda_g$, time step between snapshots $|\omega|\Delta t = 2 \cdot 10^4$, lower profiles correspond to earlier stages.

was unknown whether the solitons retain their properties with decrease in the characteristic wavelength and transition to greater amplitudes. The results of the numerical simulations presented in this paper show that the fully nonlinear equations of motion allow the existence of stable solitary waves as well, although the waves exceeding critical wave height become unstable. Numerical simulations of solitary wave collisions provide a reliable evidence that within the exact equations of motion, unlike the Benjamin-Ono equation, waves undergo a phase shift as a result of the interaction. Despite the fact that generation of oscillatory waves was observed during the collision, solitary wave amplitudes remained close to their initial values; this may indicate that the interaction is almost elastic and an approximate integrable model of this process may exist outside the range of applicability of the Benjamin-Ono equation.

In our study, we assumed deep water regime. If we consider long waves of length L with localized crests in fluid of finite

depth D , the deep water regime for them would imply that the intrinsic length scale λ_g due to vorticity ω has to be much smaller than the water depth, i.e., $\lambda_g = g/\omega^2 \ll L < 2D$. The magnitude of vorticity must be large enough to provide sufficient separation of scales between λ_g and D . Here, we take into account the fact that, as we observed in our study, for long waves there exists a critical wave height and, therefore, a minimum crest width of the order of a few λ_g ; the waves must be much longer than λ_g for their crests to be localized in a small fraction of wavelength. The condition $\lambda_g \ll D$ may be difficult to satisfy for the water waves, as it would require unrealistically large values of vorticity. An example of a geophysical process, where this requirement is easier to satisfy, is internal waves propagating zonally on equator, where constant vorticity is provided by the Earth rotation, while the effective gravitational acceleration g^* is greatly reduced. In context of geophysical applications our simulations can be viewed as a toy model aimed at understanding of this very special class of wave motions.

ACKNOWLEDGEMENTS

The authors would like to express their gratitude to V. I. Shrira and K. A. Gorshkov for providing valuable suggestions. This research was supported by the Russian Foundation for Basic Research (Grant No. 21-55-52005 MNT_a), Russian Science Foundation (Grant No. 19-17-00209) and by the President of the Russian Federation (Grant No. MK-2041.2017.5).

DATA AVAILABILITY

The data that support the findings of this study are available within the article.

Appendix A: Derivation of the Benjamin-Ono equation

We use the system of equations²²

$$y_t(1 + \tilde{x}_\xi) - x_t y_\xi - \omega y y_\xi = -\hat{H}\varphi_\xi, \quad (\text{A1a})$$

$$\begin{aligned} &\varphi_t y_\xi - \varphi_\xi y_t + g y y_\xi + \omega \psi y_\xi \\ &+ \hat{H}\{\varphi_t(1 + \tilde{x}_\xi) - \varphi_\xi x_t + g y(1 + \tilde{x}_\xi) \\ &+ \omega(\psi(1 + \tilde{x}_\xi) - \varphi_\xi y)\} = 0. \end{aligned} \quad (\text{A1b})$$

Let us consider the linearized problem:

$$\begin{aligned} y_t &= -\hat{H}\varphi_\xi, \\ g y + \varphi_t + \omega \hat{H}\varphi &= 0. \end{aligned}$$

Hence we arrive at the integrodifferential equation

$$\varphi_{tt} + \omega \hat{H}\varphi_t - g \hat{H}\varphi_\xi = 0.$$

From the dispersion relation (5), we find the linear dispersion law:

$$\Omega_{1,2} = \frac{\omega}{2} \pm \sqrt{\frac{\omega^2}{4} + gk}.$$

At $gk \ll \omega^2$ for long, weakly dispersive waves propagating against the flow ($\omega < 0$), the linear dispersion relation

$$\Omega = \frac{\omega}{2} - \frac{\omega}{2} \sqrt{1 + \frac{4gk}{\omega^2}}$$

goes to

$$\Omega = -\frac{gk}{\omega} + \frac{g^2 k^2}{\omega^3}. \quad (\text{A2})$$

(The value $c_0 = -\frac{g}{\omega}$ by the dimension represents the velocity of long waves with small amplitude).

Let us show that the evolution of nonlinear waves corresponding to the linear dispersion law (A2) is described by the Benjamin-Ono equation, whose solitons have the form of a Lorentz pulse. In the system of equations (A1) we make the substitution

$$y(\xi, t) \rightarrow y(\zeta, t), \quad \varphi(\xi, t) \rightarrow \varphi(\zeta, t),$$

where

$$\zeta = \varepsilon \left(\xi + \frac{g}{\omega} t \right), \quad \tau = -\varepsilon^2 \frac{g}{\omega} t, \quad (\text{A3})$$

and where ε is a small parameter.

Substituting (A3) into the system of equations (A1), after some algebra, we have

$$\frac{g}{\omega} y_\zeta - \varepsilon \frac{g}{\omega} y_\tau (1 + \varepsilon \tilde{x}_\zeta) + \varepsilon^2 \frac{g}{\omega} \tilde{x}_\tau y_\zeta - \omega y y_\zeta = -\hat{H} \varphi_\zeta \quad (\text{A4a})$$

$$\begin{aligned} & g y (1 + \varepsilon \tilde{x}_\zeta) + \varepsilon \frac{g}{\omega} \varphi_\zeta - \varepsilon^2 \frac{g}{\omega} \varphi_\tau (1 + \varepsilon \tilde{x}_\zeta) \\ & + \varepsilon^3 \frac{g}{\omega} \varphi_\zeta \tilde{x}_\tau - \varepsilon \omega y \varphi_\zeta + \omega \psi (1 + \varepsilon \tilde{x}_\zeta) \\ & = \hat{H} (\varepsilon^3 \frac{g}{\omega} y_\tau \varphi_\zeta - \varepsilon^3 \frac{g}{\omega} y_\zeta \varphi_\tau + \varepsilon g y y_\zeta + \varepsilon \omega \psi y_\zeta) \end{aligned} \quad (\text{A4b})$$

We seek the solution of the system (A4) in the form of a series with respect to ε :

$$y(\zeta, \tau) = \varepsilon y_1(\zeta, \tau) + \varepsilon^2 y_2(\zeta, \tau) + \dots \quad (\text{A5})$$

$$\varphi(\zeta, \tau) = \varepsilon \varphi_1(\zeta, \tau) + \varepsilon^2 \varphi_2(\zeta, \tau) + \dots \quad (\text{A6})$$

We substitute (A5) and (A6) into system (A4) and select the terms of the same orders of magnitude. In the first approximation

$$\begin{aligned} & \frac{g}{\omega} \frac{\partial y_1}{\partial \zeta} = -\hat{H} \frac{\partial \varphi_1}{\partial \zeta} \\ & g y_1 + \omega \hat{H} \varphi_1 = 0. \end{aligned}$$

In the following order

$$\frac{g}{\omega} \frac{\partial y_2}{\partial \zeta} - \frac{g}{\omega} \frac{\partial y_1}{\partial \tau} - \omega y_1 \frac{\partial y_1}{\partial \zeta} = -\hat{H} \frac{\partial \varphi_2}{\partial \zeta}, \quad (\text{A7a})$$

$$g y_2 + \frac{g}{\omega} \frac{\partial \varphi_1}{\partial \zeta} + \omega \hat{H} \varphi_2 = 0. \quad (\text{A7b})$$

System (A7) leads to the differential equation

$$\frac{g}{\omega} \frac{\partial y_1}{\partial \tau} + \omega y_1 \frac{\partial y_1}{\partial \zeta} + \frac{g}{\omega^2} \frac{\partial^2 \varphi_1}{\partial \zeta^2} = 0.$$

Considering that

$$\frac{\partial^2 \varphi_1}{\partial \zeta^2} = \frac{g}{\omega} \hat{H} \frac{\partial^2 y_1}{\partial \zeta^2},$$

we obtain the following Benjamin-Ono equation ($y_1 = y$) (omitting index 1):

$$\frac{g}{\omega} \frac{\partial y}{\partial \tau} + \omega y \frac{\partial y}{\partial \zeta} + \frac{g^2}{\omega^3} \hat{H} \frac{\partial^2 y}{\partial \zeta^2} = 0. \quad (\text{A8})$$

Using the initial variables, the equation (A8) takes the form of the equation (7).

- ¹D. Peregrine, "Interaction of water waves and currents," in *Advances in Applied Mechanics*, Vol. 16 (Elsevier, 1976) pp. 9–117.
- ²R. Thomas, C. Kharif, and M. Manna, "A nonlinear Schrödinger equation for water waves on finite depth with constant vorticity," *Physics of Fluids* **24**, 127102 (2012).
- ³M. L. Banner and O. Phillips, "On the incipient breaking of small scale waves," *Journal of Fluid Mechanics* **65**, 647–656 (1974).
- ⁴V. Shrira, "Nonlinear waves at the surface of a liquid layer with a constant vorticity," in *Dokl. Akad. Nauk SSSR*, Vol. 286 (1986) pp. 1332–1336.
- ⁵J. A. Simmen and P. Saffman, "Steady deep-water waves on a linear shear current," *Studies in Applied Mathematics* **73**, 35–57 (1985).
- ⁶A. T. Da Silva and D. Peregrine, "Steep, steady surface waves on water of finite depth with constant vorticity," *Journal of Fluid Mechanics* **195**, 281–302 (1988).
- ⁷D. Pullin and R. Grimshaw, "Finite-amplitude solitary waves at the interface between two homogeneous fluids," *The Physics of Fluids* **31**, 3550–3559 (1988).
- ⁸J.-M. Vanden-Broeck, "Steep solitary waves in water of finite depth with constant vorticity," *Journal of Fluid Mechanics* **274**, 339–348 (1994).
- ⁹J.-M. Vanden-Broeck, "Periodic waves with constant vorticity in water of infinite depth," *IMA Journal of Applied Mathematics* **56**, 207–217 (1996).
- ¹⁰S. A. Dyachenko and V. M. Hur, "Stokes waves with constant vorticity: I. numerical computation," *Studies in Applied Mathematics* **142**, 162–189 (2019).
- ¹¹S. A. Dyachenko and V. M. Hur, "Stokes waves with constant vorticity: folds, gaps and fluid bubbles," *Journal of Fluid Mechanics* **878**, 502–521 (2019).
- ¹²Y. Matsuno, "Exact multi-soliton solution for nonlinear waves in a stratified fluid of finite depth," *Physics Letters A* **74**, 233–235 (1979).
- ¹³Y. Matsuno, "Interaction of the Benjamin-Ono solitons," *Journal of Physics A: Mathematical and General* **13**, 1519 (1980).
- ¹⁴V. Ruban, "Explicit equations for two-dimensional water waves with constant vorticity," *Physical Review E* **77**, 037302 (2008).
- ¹⁵W. Choi, "Nonlinear surface waves interacting with a linear shear current," *Mathematics and Computers in Simulation* **80**, 29–36 (2009).
- ¹⁶V. E. Zakharov, A. I. Dyachenko, and O. A. Vasilyev, "New method for numerical simulation of a nonstationary potential flow of incompressible fluid with a free surface," *European Journal of Mechanics-B/Fluids* **21**, 283–291 (2002).
- ¹⁷A. S. Dosaev, Y. I. Troitskaya, and M. I. Shishina, "Simulation of surface gravity waves in the Dyachenko variables on the free boundary of flow with constant vorticity," *Fluid Dynamics* **52**, 58–70 (2017).
- ¹⁸M. Tanaka, "The stability of steep gravity waves," *Journal of the Physical Society of Japan* **52**, 3047–3055 (1983).
- ¹⁹M. Longuet-Higgins and M. Tanaka, "On the crest instabilities of steep surface waves," *Journal of Fluid Mechanics* **336**, 51–68 (1997).

- ²⁰S. Murashige and W. Choi, “Stability analysis of deep-water waves on a linear shear current using unsteady conformal mapping,” *Journal of Fluid Mechanics* **885**, A41 (2020).
- ²¹P. M. Lushnikov, S. A. Dyachenko, and D. A. Silantiev, “New conformal mapping for adaptive resolving of the complex singularities of Stokes wave,” *Proceedings of the Royal Society A: Mathematical, Physical and Engineering Sciences* **473**, 20160101 (2016).
- ²²M. I. Shishina, “Steady surface gravity waves on a constant vorticity flow free surface,” *Processes in Geomedia. Special Issue* **8**, 71–77 (2016).
- ²³T. B. Benjamin, “Internal waves of permanent form in fluids of great depth,” *Journal of Fluid Mechanics* **29**, 559–592 (1967).